# The northeastern Algeria hydrothermal system: gravimetric data and structural implication

Yasser Bayou[1,2]* , Abdeslam Abtout[2], Rosemary A. Renaut[3], Boualem Bouyahiaoui[2], Said Maouche[2], Saeed Vatankhah[4] and Mohamed Cherif Berguig[1]

*Correspondence:
yasser.bayou35@gmail.com

[1] FSTGAT, University of Science and Technology Houari Boumediene, BP 32, El-Alia Bab Ezzouar, 16111 Algiers, Algeria
[2] CRAAG, Research Center of Astronomy, Astrophysics and Geophysics, BP 63 Bouzaréah, 16340 Algiers, Algeria
[3] School of Mathematical and Statistical Sciences, Arizona State University, Tempe, AZ, USA
[4] Institute of Geophysics, University of Tehran, District 6, Tehran, Tehran, Iran

## Abstract

The Tell Atlas of Algeria has a huge potential for hydrothermal energy from over 240 thermal springs with temperatures up to 98° C in the Guelma area. The most exciting region is situated in the northeastern part which is known to have the hottest hydrothermal systems. In this work, we use a high-resolution gravity study to identify the location and origin of the hot water, and how it reaches the surface. Gravimetric data analysis shows the shapes of the anomalies arising due to structures at different subsurface depths. The calculation of the energy spectrum for the data also showcases the depths of the bodies causing anomalies. 3D-Euler deconvolution is applied to estimate the depths of preexisting tectonic structures (faults). These preprocessing steps assist with assessing signal attenuation that impacts the Bouguer anomaly map. The residual anomaly is used in a three-dimensional inversion to provide a subsurface density distribution model that illustrates the locations of the origin of the dominant subsurface thermal systems. Overall, the combination of these standard processing steps applied to the measurements of gravity data at the surface provides new insights about the sources of the hydrothermal systems in the Hammam Debagh and Hammam Ouled Ali regions. Faults that are key to the water infiltrating from depth to the surface are also identified. These represent the pathway of the hot water in the study area.

**Keywords:** Northeastern Algeria, Hydrothermal system, Gravimetric data, 3D gravity model

## Introduction

Worldwide, geothermal systems are known for their geological heterogeneities and complex configurations (Zhao et al. 2020; Peacock et al. 2020). Studies of hot geothermal sources have recently increased, and several quantitative methods have been developed and used to provide details about these geothermal sources. Such analyses provide significant steps toward both understanding the origins of these systems and their use as an energy resource. The environmentally friendly energy obtained from geothermal systems can be used for electricity generation, cooling, and aquaculture (Dickson and

Bayou *et al. Geothermal Energy*     (2023) 11:14

Page 2 of 26

Fanelli 2013). The most important hydrothermal systems around the world are located on active marginal faults associated with subduction zones which explain the deep magmatic origins of the hot water (Risacher et al. 2011).

The African continent is known to have many randomly scattered hydrothermal hot spring spots (Armadillo et al. 2020; Leseane et al. 2015). Most geothermal systems are located in the eastern part of the continent and along the north coast (Elbarbary et al. 2022). The investigation of geothermal systems has been performed in several fields. In particular, the analysis of the chemical composition of the spring water indicates the source and depth of the system. Generally, water is warmed over magma rocks (igneous rocks) and reaches the surface using a network created by faults. These network systems are specific to the seismotectonic features of the region where the hot spot is located (Amara et al. 2019; Maouche et al. 2013). These features allow the rapid upflow of water to the surface. The pressure created by the water energy can also create new routes to the surface.

The Tell Atlas of Algeria is located on the northern edge of the African continent. It is characterized by complex geology related to the compressional tectonics in the continental domain and guided by the convergent movement of Africa towards Eurasia (Meghraoui and Pondrelli 2012; Maouche et al. 2019). The geological structures are folds, thrusts and overthrusts, and nappes that prevail in this part of the orogenic Alpine belt [Maghrebides belt, Fig. 1 region (a)]. The E–W elongation of tectonic structures is highlighted with a magmatic lineament (activity) from Ras Tarf in Morocco to the north of Tunisia (Abbassene et al. 2016). This part of Africa is a significant active zone with a permanent seismicity (Yelles-Chaouche et al. 2006; Bendjama et al. 2021) and is known for its more than 240 hydrothermal springs (Amara et al. 2019; Maouche et al. 2013; Belhai et al. 2015; Bouchareb-Haouchine et al. 2012). They are divided into mesothermal and hydrothermal springs. The first exploration of these geothermal systems as a geothermal resource was originated by an Algerian state-owned group in 1967 (Lebbihiat et al. 2021; Saibi 2009). The temperatures of these systems range between 20° C and 97° C (Belhai et al. 2015), and the estimated potential energy production along these Algerian hot spots accounts for about 54.64 MW (Saibi 2009; Ouali et al. 2018). Despite the considerable availability of this eco-energy, Algeria exploits only about 18% (10.28 MW) of this resource.

The Guelma region (Mio-Plio-Quaternary sedimentary basin, northeastern Algeria) is recognized for its high-water temperature resulting from an intense geothermal gradient. This effect is evidenced by the large number of hot springs, with variable temperatures, that emerge in the area. The temperature depends on both the location and the depth of the water source. The pattern that reveals the location and upflow of water in the area is represented by travertine deposits. The travertine outlines the historical path of hot water and its components. Geochemical interactions assure that most hydrothermal sources reach the surface with a stable temperature. Geothermal sources in the western part of the Guelma basin contain carbonic and sulfur gas (Bouaicha et al. 2019), and the travertine deposits in the region describe the patterns of these hot spring locations. These travertine deposits primarily indicate the path of the active neotectonic (Maouche et al. 2013). They might also indicate sealed fracture systems through which geothermal brines are discharged on the surface. Most of the hot spring spots in the region are
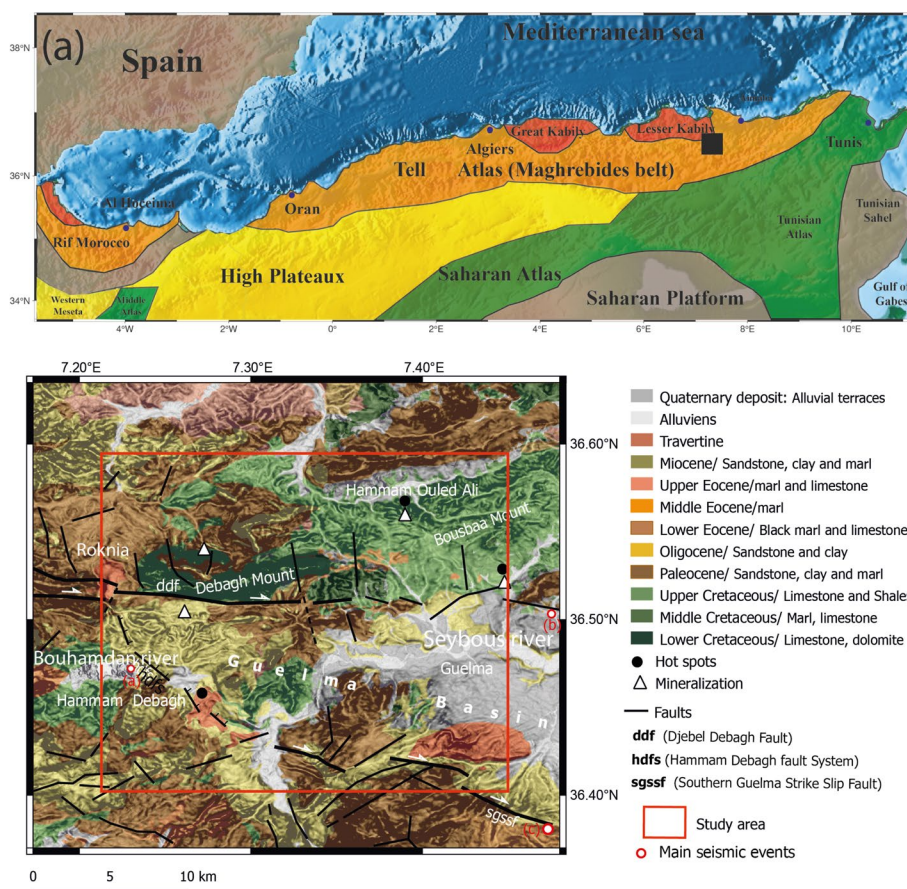
**Fig. 1** The geological map of the study area that involves Hammam Debagh, Hammam Ouled Ali, and Djebel Bousbaa (Bousbaa Mountain) is illustrated in the lower panel. This geological map was obtained using a combination of multiple maps with a uniform scale of 1/50000. The white triangles represent locations of extracted mineralization (Amara et al. 2019). The black line represents the known faults in the region (Amara et al. 2019). The black circles represent the hot geothermal systems in the area. Region (a) in the upper panel shows the structural map of the North of Algeria, and the black square on the map represents the study area

focused along active faults. Geologically, this famous hot spring area sits in the western part of the Plio-Quaternary intra-mountainous Guelma basin, which is described by a major fault of the Hammam Debagh [Fig. 1 region (b)].

The acquired gravimetric survey data provide the first opportunity to obtain information on the hydrothermal system of the Hammam Debagh and Hammam Ouled Ali areas. Here, the presented gravimetric study illustrates the geological heterogeneity and the subsurface configuration of this hydrothermal complex system. The specific study area contains three hot spring sites [Hammam Debagh, Hammam Ouled Ali and Djebel Bousbaa (Bousbaa Mountain)] (Fig. 1). Quantitative processing of the Bouguer anomaly provides information on the locations and shapes of the bodies that generate the specific anomalies and are related to upflow of the geothermal fluid sources of the thermal springs.

The gravity data were acquired using a terrestrial Scintrex CG3 from 2021/10/08 to 2021/10/26, and the coordinates were obtained using a bi-frequency GPS (Leica). A total of 470 gravimetric measurements were made. This data was tied to the Algerian absolute

Bayou *et al. Geothermal Energy*      (2023) 11:14

Page 4 of 26

gravity network (Bayou et al. 2022). A new data set was acquired along the Hammam Debagh and Hammam Ouled Ali areas, with a spacing of approximately 1 km between gravimetric measurements. Locally, at Hammam Debagh the measurement stations were approximately 200 m apart. The analysis of such data sets provides insights about the sources of hydrothermal systems. The details revealed from the 3D inversion of the residual gravity anomalies delineate the locations of high and low densities in the region. The obtained density contrast provides information on the neotectonic activity in the region.

## Geological setting

The Tell Atlas of Algeria hosts a significant unknown geological event arising from major structural processes during the Cenozoic period (Maouche et al. 2011). The neotectonics features correspond to E–W to NE–SW trending folds and reverse faults, affecting Quaternary deposits (Bouyahiaoui et al. 2015; Maouche et al. 2013; Meghraoui 1988; Bousquet 1986). Generally, Algeria's Quaternary deposit is an integral part of the geologic setting of the study area (Vila 1980). Located at the easternmost of the north of Algeria, the Guelma Basin presents as a vast depression, elongated E–W and bordered, to the North and South, by reliefs made up of allochthonous formations, belonging to the Tellian domain [Fig. 1 region (b)]. Similar to all the northern Algeria basins, the Guelma plain is an intra-mountainous post-Neogene basin, but with the particular feature of being a "pull apart" type basin that is tectonically very active. It is also located along a major strike-slip accident limited by border faults which are situated in the east and south of the study area, respectively. These faults produced major seismic events (the most recent of these were 12/21/1980 Ms = 5.2, 09/20/2003 Ms = 4.8 and 01/19/1997 Ms = 4.0) that are related to significant hydrothermal activity in the region, evidenced by the presence of several hydrothermal stations such as those of Hammam Debagh and Hammam Ouled Ali.

The Guelma basin is a basin of the pull-apart type that was formed during the post-nappe period and filled by Miocene and Plio-Quaternary sediment (Vila 1980; Meghraoui 1988). It is well-known as a Neogene area bounded by major faults. The basement is characterized by carbonate rocks from Jurassic and Cretaceous on which tertiary formations are deposited (Vila 1980; Raoult 1974). The deposits of this Neogene basin are divided into two sequences; shallow depths (Tortonian period), and sandstone interstratified with marl, clays conglomerates and limestone in a line of successions. Furthermore, the Quaternary deposits are represented particularly by alluvial terraces related to the major rivers (Bouhamdan and Seybous rivers) (Maouche et al. 2019). The northern part of this basin is identified as Cretaceous of Djebel Bousbaa (Bousbaa Mountain) which consists of marl and limestone (Lahondère 1987; Vila 1980). This series is described with a similarity to the ultra-Tellian compound.

The surrounding area of the Guelma basin is well known for its travertine deposits. These deposits provide an efficient network for the flow of the hydrothermal system (Bouyahiaoui et al. 2017; Belhai et al. 2015). The area of hydrothermal systems is derived from Miocene to Quaternary deposits and topped with high-density alluvium deposits that are well known to be highly permeable (unconsolidated conglomerates). As such, these deposits allow rainwater infiltration and flow of hot water from the geothermal

Bayou *et al. Geothermal Energy*     (2023) 11:14

Page 5 of 26

systems. The rainwater seeps through the deep bodies, and is warmed at depth by a heat source. Subsequently, the water arriving at the surface is hot. Most hydrothermal systems have a common origin that depends on the local geology of the region.

## Data acquisition and processing

### Gravity measurements

To better understand the hidden subsurface geological heterogeneity of the geothermal systems of Hammam Debagh and Hammam Ouled Ali areas, new gravity measurements were acquired. The resulting gravimetric map is used to determine the deep structure and provide gravimetric evidence of the hydrothermal system of the study area. The gravity data set was collected from 2021/10/08 to 2021/10/26, using a terrestrial gravimeter model Scintrex CG3. The complete dataset consists of 470 gravity stations, and covers a total area of about 400 km$^2$. It covers the edge of the Guelma basin and the hydrothermal systems of Hammam Debagh and Hammam Ouled Ali. The gravimetric measurement stations were spaced approximately 1 km apart. Locally, at Hammam Debagh the measurement stations were spaced approximately 200 m apart.

To control for instrumental drift and assess the quality of the measurements, the data are tied to the relatively new gravimetric network in the northeastern part of Algeria (Bayou et al. 2022). This network is tied to the Algerian absolute gravity network (Francis, 2003). To perform the gravimetric corrections, we determined the coordinates and altitude of each measurement station using a bi-frequency differential GPS Leica GS-10. Several quality control steps were applied to the acquired data. Repeat measurements were made for 10 % of the data. The differences between the two sets of measurements follow a Gaussian distribution with a mean of about 10 $\mu$ Gal. The observed gravity measurement was calculated using the relative differences of the device reading converted to absolute gravity value, after correcting for tidal effect and instrumental drift. The conversion to absolute value was obtained by linking the gravimetric readings to the gravity references stations. The moon–solar correction for our data is a built-in instrument calculation that is performed by introducing the measurement time and the geographical coordinates of the prospected area. The daily instrumental drift is assumed linear and is divided proportionally between the daily gravity measurements. The obtained pre-processed data are used to calculate the Bouguer anomaly (BA). The BA provides critical evidence of the gravimetric field. The values, $g_{\mathrm{BA}}$, of the BA at each data location are calculated using the non-linear map given by the following formula:

$$g_{\mathrm{BA}} = g_{\mathrm{obs}} - g(\phi) + (0.3086\,h_{\mathrm{s}}) - (0.0419d\,h_{\mathrm{s}}) + g_{\mathrm{T}}. \qquad (1)$$

Here, $g_{\mathrm{obs}}$ is the observed gravity measurement at a given station (mGal), $g(\phi)$ represents the theoretical gravity computed following the IUGG1967 system (mGal), $h_{\mathrm{s}}$ is the elevation at the measurement station (in meters), $d$ represents the density correction, and $g_{\mathrm{T}}$ is the topographic correction (mGal).

After calculating the BA for the complete data set, which is not on a uniform grid, the BA is interpolated to a uniform grid for qualitative and quantitative interpretation (Fig. 2). There are many options for the interpolation, as noted in Enriquez et al. (1983), but we chose to use the method of minimum curvature which is a standard choice in the literature (Mickus et al. 1991). Further, unless specifically noted, for the data processing
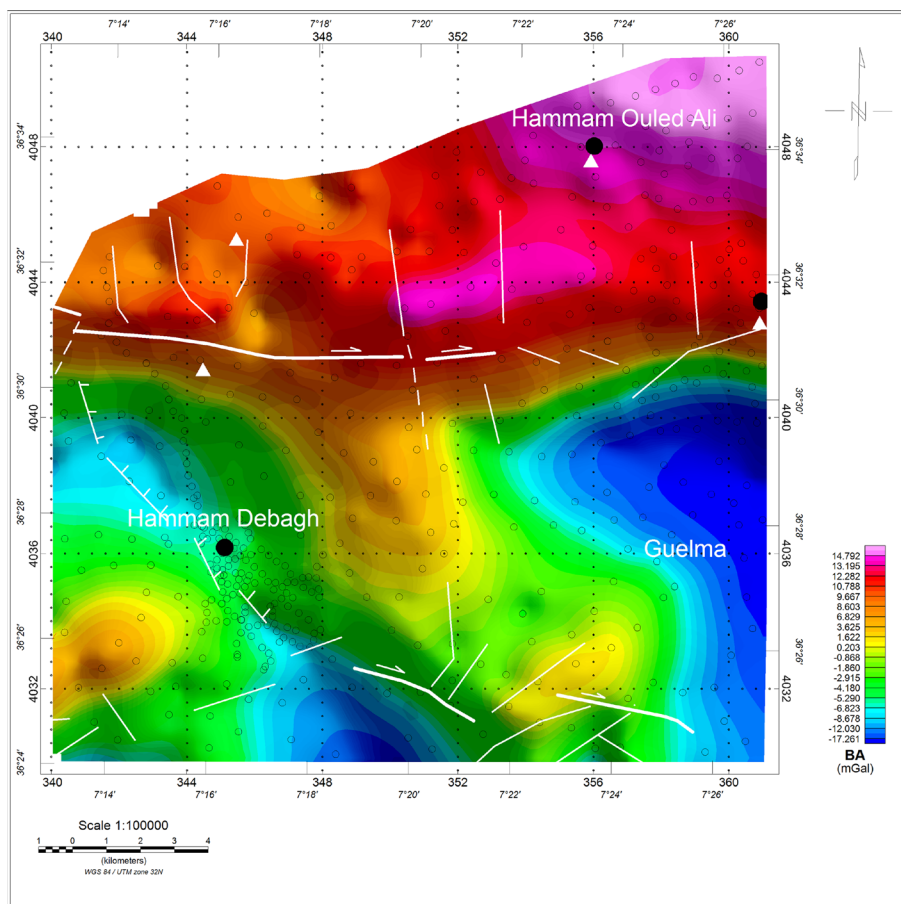
Bayou *et al. Geothermal Energy* (2023) 11:14

Page 6 of 26



**Fig. 2** The Bouguer Anomaly of the study area. The black circles represent the gravimetric measurements. The black points represent the hot geothermal systems in the region. The white triangles represent the mineralization in the area (Amara et al. 2019). The white lines represent the geological faults into the area. The gravity map was calculated assuming a density of 2500 kg/cm$^3$

of the gravimetric data we use the Geosoft Oasis Montaj® software package, where we indicate in each case the equations used and point to the relevant references, noting that a good overview is in Blakely (1995). Finally, for obtaining the BA we assume a background density of 2500 kg/cm$^3$ which is a suitable estimate for a sedimentary basin that consists of Miocene to Quaternary deposits (Basantaray and Mandal 2022). The resulting values of the BA on the uniform grid are indicated throughout by $g_{BA}$.

The Bouguer anomaly map drawn for the geothermal system region shows values ranging from $-22.300$ to $17.802$ mGal (Fig. 2). It reveals a smooth variation of anomalies around the hot spots, some of which are prominent. This map shows a progression of the gravity field from south to north. The set of E−W elongated high anomalies located in the north corresponds to Hammam Ouled Ali, Djebel Debagh (Debagh Mountain) structures, corresponding to Cretaceous and Paleocene geological formations. The low anomalies in the southeast correspond to the Guelma sedimentary basin comprising Plio-Quaternary and Quaternary deposits. The southwestern zone indicates that there is an NW–SE elongated low anomaly. It corresponds to the presence of alluvian, travertine and Miocene deposits. A NW–SE high anomaly set is next to the Hammam Debagh

(the geothermal system location) and limits to the west the Guelma sedimentary basin that comprises Paleocene formations. To the southwest of the Hammam Debagh area, the Cretaceous deposits are marked by gravimetric maxima elongated in the NE–SW direction (Fig. 2)

**Separation of anomalies**

The BA map for the study area contains all full lateral and horizontal effects (superficial, intermediate and deep). To obtain further details that describe the anomalies at different depths, and to isolate the signals due to low and high frequencies, it is necessary to apply multiple additional processing steps of the BA. This usually starts with the elimination of the regional effects from the BA, and is accomplished using polynomial fitting of different orders to separate the local and global components (Oldham and Sutherland 1955). The obtained residual anomalies are pivotal for the inversion process that is used to determine the density distribution in the subsurface. Here, we use polynomials of different orders (Oldham and Sutherland 1955; Mickus et al. 1991), yielding the approximate measured field as a polynomial in $x$ and $y$, corresponding to East and North directions, respectively. The polynomial, $P(x, y) = \sum_{i=1}^{n} a_i P_i(x, y)$, is selected to provide the anomaly that best matches the regional map. The $P_i(x, y)$ are the basis polynomials in $x$ and $y$ corresponding to all products of the basis polynomials in $x$ and $y$ (1, $x$, $y$, $x^2$, $xy$, $y^2$, etc.) and the $a_i$ are the real coefficients of the polynomial $P(x, y)$. In this case, we used the polynomial of order $n = 1$ to retrieve the local regional anomaly, given by $P(x, y) = a + bx + cy$, where $a = -8.655$, $b = -0.206$ and $c = 1.207$, from which we then obtain the residual anomaly $g_{RA}(x, y) = g_{BA}(x, y) - P(x, y)$, shown in Fig. 3A and B, respectively. This is justified by the subsequent examination of the upward continuation map at 5000 m (Fig. 4).

The regional anomaly map shows a regular decrease in the gravitational field from North to South (Fig. 3A). This gravity gradient presents a slope of about of 1 mGal/km. The residual anomaly map (Fig. 3B) enhances the local anomalies shown on the Bouguer anomaly map, the tendency is mainly a series of high anomalies surrounded in the East (Guelma) and West (Hammam Debagh) alternating with low anomalies. The values of the gravity field range between −19.206 and +10.513 mGal and delineate areas with different density rocks. Three major positive anomalies are observed; the first-one is a positive anomaly (A1, Fig. 3B) in the north of the Guelma basin, with E–W direction; representing the Djebel Bousbaa (Bousbaa Mountain) and Debagh Mountains. This positive anomaly is related to allochthonous Cretaceous formations. The second positive anomaly (A2, Fig. 3B) in the South, elongated in the NW–SE direction, separates the Guelma basin and the Hammam Debagh area. It corresponds to Paleocene formations. The third positive anomaly (A3, Fig. 3B) in the southwest of Hammam Debagh is characterized by Cretaceous and Paleocene formation deposits. In addition, a positive anomaly (A4, Fig. 3B) is located northeast Hammam Debagh and corresponds to allochthonous Cretaceous formations. The negative anomaly (Neg1) is associated with the sedimentary series in the Guelma basin, while the negative anomaly (Neg2) corresponding to the Miocene series suggests the extension of the basin towards the
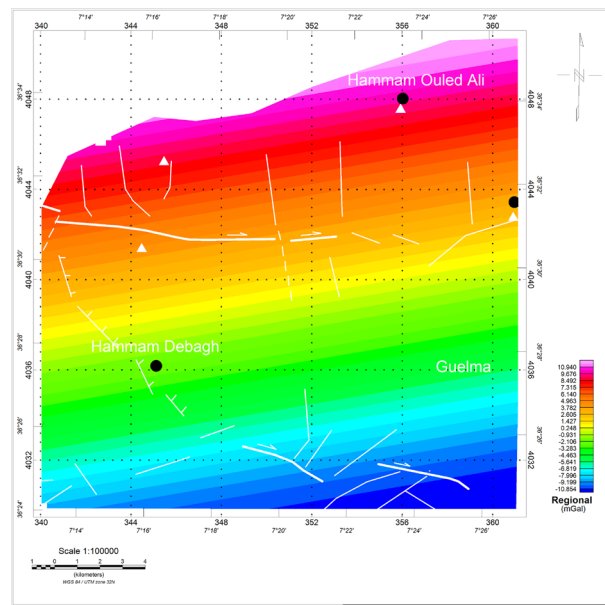
(A)
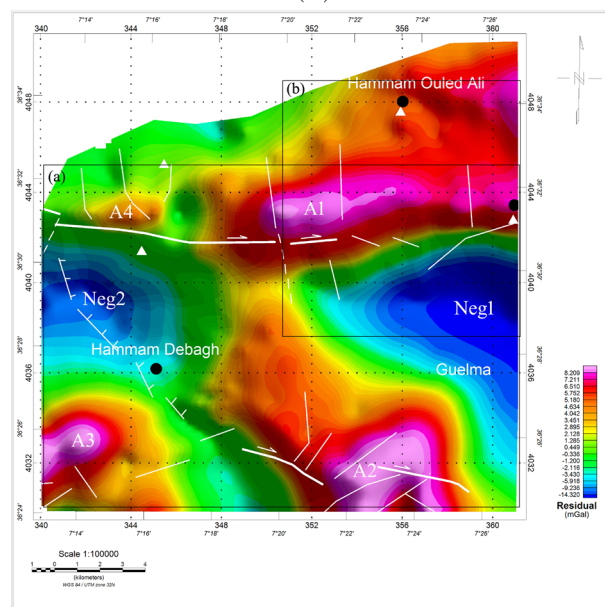


(B)

**Fig. 3** **A** The regional anomaly and **B** the residual anomaly calculated from the Bouguer anomaly. The white lines represent the geological faults into the area. The black points represent the hot spring locations, and the white triangles represent locations of significant mineralization in the area (Amara et al. 2019)

West. For further processing, the region covered by the residual anomaly is divided into two rectangular regions [Fig. 3B (a) and (b)] for which the first is larger than the second.

In order to identify the gravity lineaments, we calculated the vertical and horizontal gradients, (Fig. 5A and B, respectively), for the potential field data, namely for the BA (Baranov 1953; Aydogan 2011). Gradient filters (identifying edge locations) are used to determine the water infiltration and to identify the key to the upwelling
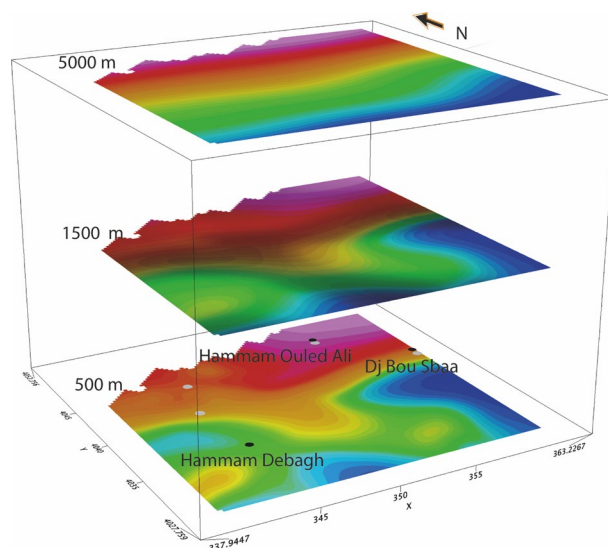
**Fig. 4** Upward continuation applied to the Bouguer anomaly. The three maps in the cube illustrate the upward continuation from depths of 500 m, 1500 m and 5000 m, respectively

water on the surface. Gradient filtering also assists with finding different faults and geological contacts with different density. Edge filters highlight vertical and geologic heterogeneity (Bendali et al. 2022). It is clear that horizontal gradients, within the plane of the potential field, can be found by direct convolution for East–West and North–South derivatives (Blakely 1995, Chapter 12, Equation 12.49). Vertical gradients can also be found by applying Laplace's equation for the potential field, the BA, $g_{BA}$ (Blakely 1995, Section 12.2). Hence, to calculate the horizontal gradient (in plane) we use the convolution approach described in Aydogan (2011), Blakely (1995) with the East–West and North–South masks, and a threshold applied. For the vertical gradients the approach also uses the Fourier transform convolution and inversion, with thresholding, as indicated in Blakely (1995, Section 12.2).

The gradient maps (Fig. 5A and B) show an important series of NW–SE elongated gradient highs that correlate with the limits of the anomalies described (i.e., A1, A2, A3, and A4 in Fig. 3B) with some conjugate faults shown by NNE–SSW anomalies. The Guelma basin is limited in its northern parts by anomalies elongated in E–W to NNE–SSW directions. The area around the Hammam Debagh area to west of the Guelma basin is marked by a NW–SE fault system (i.e., Hammam Debagh fault). The Hammam Debagh area is characterized by a series of NW–SE gravimetric lineaments and is recognized for strong seismic activity along the Hammam Debagh fault, which was the site of the 1937 Hammam Debagh earthquake. The Hammam Ouled Ali area is delineated by NW–SE lineaments, where intense micro-seismic activity has been recorded. We note also that the positions of the mineralization and hot hydrothermal springs coincide with zones of high gradients.

To enhance the long wavelength anomalies, we applied the upward continuation method at different altitudes (Bhattacharyya and Chan 1977; Gibert and Galdeano 1985). Upward continuation is considered a clean filter because it produces almost no side effects. Thus no correction filtering or other processing is needed. Consequently,
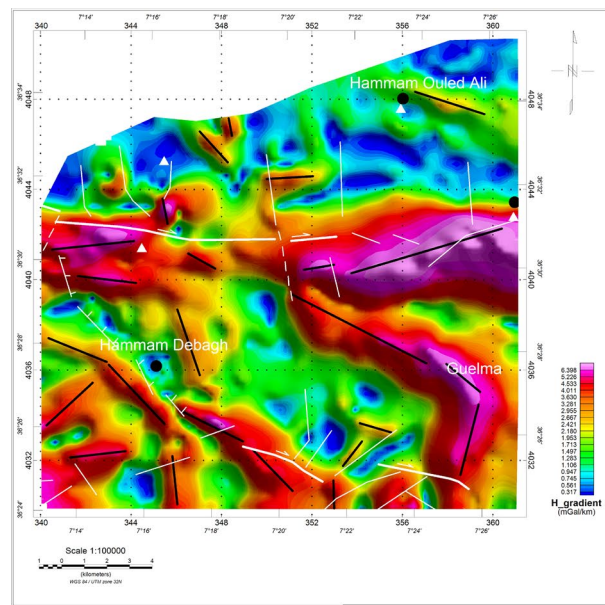
(A)
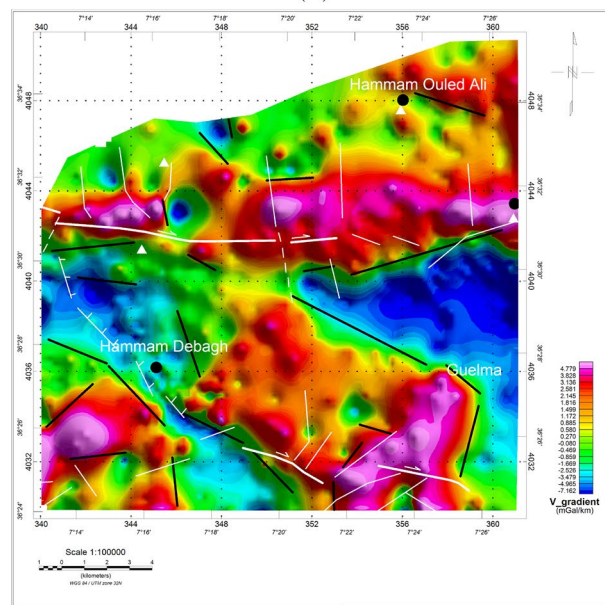


(B)

**Fig. 5 A** The horizontal gradient and **B** the vertical gradient applied to the Bouguer anomaly. The black lines represent the gravimetric lineaments. The white lines represent the geological faults into the area. The black points represent the hot spring locations, and the white triangles represent locations of significant mineralization

upward continuation is often used to remove or minimize the effects of shallow sources and noise on the grid. Moreover, upward-continued data can be interpreted numerically with modeling programs. This is not the case for many other filtering processes. The upward continuation at different altitudes is calculated by taking the Fourier transform of the potential field, convolving with the continuation operator
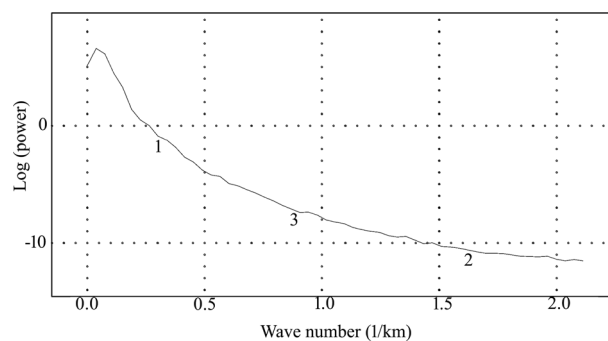
**Fig. 6** The energy spectrum extracted from the Bouguer anomaly, with three significant energy levels indicated

for height $h$ and then taking the inverse transform. This is described in Blakely (1995, Equations 12.4–12.8) and implemented using the Geosoft package.

The upward continuation map shows the anomalies of the Bouguer anomaly. Upward continuation was calculated for several heights. Here, we show the 2D horizontal slices obtained by upward continuation at depths at 500 m, 1500 m and 5000 m (Fig. 4). These upward continuation maps show an attenuation of short wavelength anomalies. At 5000 m elevation, a linear decrease in the gravitational field from North to South is obtained, which is similar to the regional anomaly for a polynomial of order 1, and justifies our choice of the order 1 polynomial filter for the regional anomaly.

**Depth estimation and modeling**
In order to determine and identify the causative bodies that generate the anomalies complementary methods of inversion and modeling are applied.

*Energy spectrum*
We calculate the energy spectrum of the BA (Spector and Grant 1970; Johnson and Macleod 2016) from which it is possible to obtain information about the main deep structures that cause the anomalies, shown in Fig. 6. The energy spectrum is written conventionally as the square of the modulus of the Fourier transform of the gravitational field (Spector and Grant 1970). The resulting spectrum is drawn on a logarithmic scale (Bouyahiaoui et al. 2017; Basantaray and Mandal 2022). The slope of the logarithmic energy spectrum is proportional to the source depth. We used the curve representing signal energy (power of the signal in the Fourier domain) as a function of frequency after calculating the statistical mean of the spectral density of the anomalies. The depth $h$ for the structure is given by $h \approx \frac{\Delta \log E}{4\pi \Delta \ell}$. Here $\Delta \log E$ stands for the log variation of the energy (power) in the $\Delta \ell$ frequency interval (measured in $km^{-1}$), and $h$ represents the depth of the body causing the anomaly (Blakely 1995, Chapter 11).

*3D-Euler deconvolution*
To better characterize anomalies and tectonic lineaments of the hydrothermal system of the Hammam Debagh and Hammam Ouled Ali areas, 3D-Euler deconvolution (Thompson 1982; Reid et al. 1990; Mikhailov et al. 2003) has been applied to the gradients of the BA, shown in Fig. 7. Improved identification of the geological
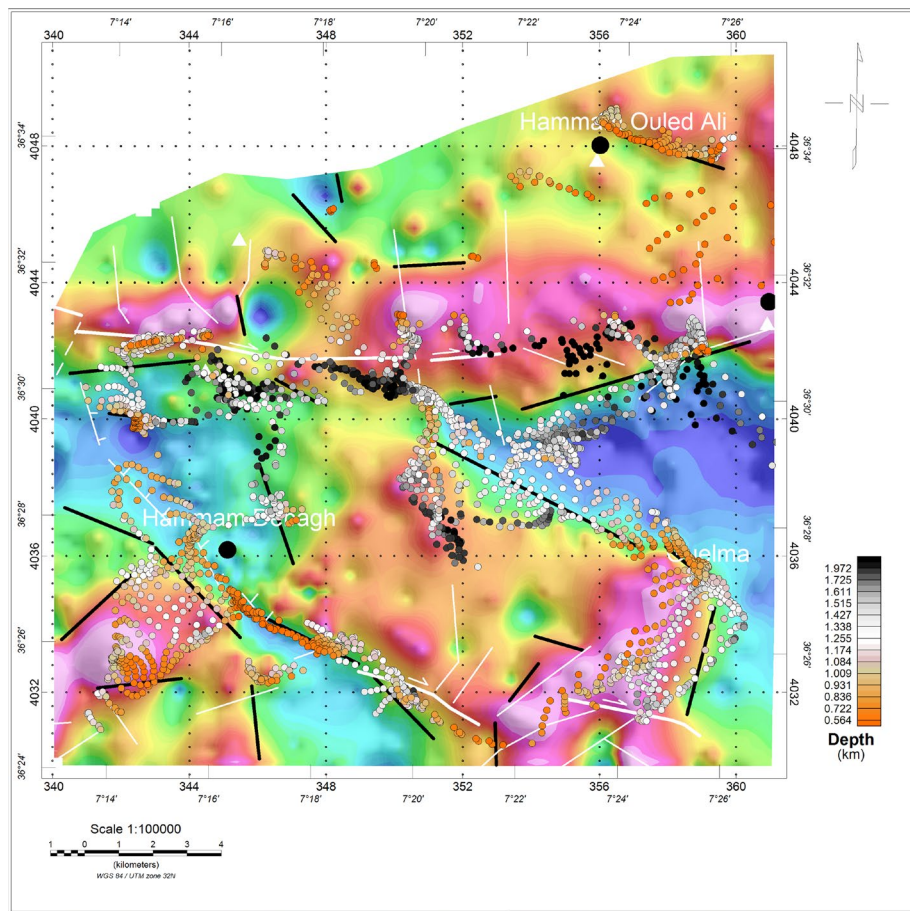
**Fig. 7** The solutions obtained by 3D-Euler deconvolution overlapped on the vertical gradient map. The white lines represent the geological faults into the area. The map is obtained with a structural index of 0.25, window size of 12, and a tolerance of 10%

fault features (location and depth) requires the implementation of the 3D-Euler deconvolution method in several cases (Alatorre-Zamora et al. 2020). The source depth is automatically estimated by this method. In addition to depth, 3D-Euler deconvolution provides an indication of the source type by structural index. This structural index is applied when performing the 3D-Euler deconvolution. For the regional interpretation of gravity data, structural indices of 0, 0.5, 1.0 and 2.0 are common for the identification of faults, contacts, sill and dyke locations (Melo and Barbosa 2017). The structural index is a measure of the rate of change of potential field with distance. The basic principle of structural index is Euler's equation of homogeneity (Reid et al. 1990) expressed for potential field analysis as:

$$(x - x_0)\left(\frac{\partial F}{\partial x}\right) + (y - y_0)\left(\frac{\partial F}{\partial y}\right) + (z - z_0)\left(\frac{\partial F}{\partial z}\right) = N(B - F). \tag{2}$$

Here, $(x_0, y_0, z_0)$ is the position of the source of the anomaly whose vertical component of potential field $F$ ($g_{\mathrm{BA}}$) is measured at $(x, y, z)$. $N$ is the structural index and $B$ is the regional value of the gravity field (Reid and Thurston 2014). The structural index is calculated by determining how many infinite dimensions, say $S$, are present in a geologic

representation (Thompson [1982](#)). The representative structural index is $N_{\max} - S$ where $N_{\max}$ is the maximum structural index for the field, $N_{\max} = 2$ for the gravity potential field which dies off quadratically from a point source (Kearey et al. [2002](#)). There are possible geologic interpretations for a particular structural index for gravity potential field data. A structural index of 0.5 is associated with the geologic model of a sill, dyke or step while a structural index of 1.0 is associated with a pipe like model (Thompson [1982](#)). A structural index of 2.0 generates relatively deeper solutions compared to structural indices of 0.5 and 1.0 and is associated with a geological model of a sphere. As suggested in Reid and Thurston ([2014](#)) the unknowns in Eq. ([2](#)) are found by applying a window to the grid domain, and solving for all unknowns in the window, given the calculated derivative values on the grid, already identified for the lineament analysis discussed above.

In this work, we are looking for the lineament; so many tests have been performed by varying different parameters for structural index, window size and tolerance. The estimate of the structural index is unstable even in the presence of a weak amount of noise and 3D-Euler deconvolution of noisy data leads to an underestimation of structural index and depth (Florio and Fedi [2014](#)). Equation ([2](#)) shows that if an undetermined regional level is present, the structural index cannot be estimated directly. In that case it should be obtained from knowledge of the geological and structural context or be chosen after a series of tests depending on the quality of the result (well grouped solution, low estimation errors, etc.). We determine the source depths and structural indices of a list of anomaly locations. The anomaly locations are generally produced using an automatic peak-finding routine which locates peaks. The depth and structural index are then calculated at these locations using the AN-EUL method (Salem and Ravat [2003](#)). The analysis of these results shows that a low structural index (equal and/or near to zero) underestimates the depths. The calculation was performed by choosing a window size equal to 12 and a 10% tolerance. As we are interested in gravity contacts, we look for structural index values with an average around 0.25. This range of structural indices produces a better grouping of the solutions and provides estimates of depths that are close to the values determined by the other methods.

### 3D inversion

The inversion of the residual anomalies for regions (a) and (b) (delineated in Fig. [3](#)B) uses the method originally described in Vatankhah et al. ([2018](#)) that was extended to be efficiently implemented using the structure of the sensitivity matrix (Hogue et al. [2020](#); Renaut et al. [2020](#)). The model for the residual anomaly for gravity data is given by

$$\mathbf{d} = \mathbf{Gm}. \tag{3}$$

Here, $\mathbf{d}$ is the vector of observed data describing the residual anomaly (denoted by $g_{\mathrm{RA}}$) and $\mathbf{G}$ is the sensitivity matrix that maps the subsurface density values $\mathbf{m}$ to the data. Matrix $\mathbf{G}$ is of size $m \times n$. This corresponds to the measured data reshaped to a column vector of length $m$ and the subsurface density values in the volume reshaped to a column vector of length $n$. The details for constructing $\mathbf{G}$ for a given configuration are carefully described in Hogue et al. ([2020](#)) and software for obtaining the matrix given a

uniform grid of measurement stations and a uniform volume discretization is available in Hogue et al. (2020). Note that in describing the forward model and inversion, we use the notation in the referenced literature.

The forward model given by the matrix Eq. (3) is under-determined, $m \ll n$ and the problem is ill-posed. This is a well-known problem for the inversion of potential field data (Boulanger and Chouteau 2001; Li and Oldenburg 1998). To obtain a stable solution it is standard to introduce a stabilizing term, also called a regularization term, and obtain the density distribution that satisfies

$$\mathbf{m} = \underset{\mathbf{m}}{\operatorname{argmin}} \left\{ \|\mathbf{Gm} - \mathbf{d}\|_2^2 + \alpha^2 \|\mathbf{m} - \mathbf{m}_0\|_r^r \right\}. \tag{4}$$

Here we use the regularizer with $r = 1$, which will provide a solution that is compact but not over smoothed, as would be obtained using the standard Tikhonov regularization with $r = 2$. The vector $\mathbf{m}_0$ is used if there is prior information on the solution that can be imposed. Equation (4) does not admit a closed form solution. Therefore, we follow the presentation in Vatankhah et al. (2018), Renaut et al. (2020) in which a solution is found iteratively using the weighted norm, via

$$\mathbf{m}^{(k)} = \underset{\mathbf{m}}{\operatorname{argmin}} \left\{ \left\|\mathbf{G}W_{\text{depth}}\mathbf{m} - \mathbf{d}\right\|_{W_{\text{d}}}^2 + \alpha_k^2 \left\| W^{(k-1)}(\mathbf{m} - \mathbf{m}^{(k-1)}) \right\|_2^2 \right\}, \tag{5}$$

where superscript $k$ indicates the iteration $k$, initialized with $\mathbf{m}^{(k)} = \mathbf{m}_0$, here taken to be zero, and we iterate to find the solution for increasing integers $k = 1, 2, \cdots, K$. Here we impose $k \leq K_{\max}$, where $K_{\max}$ is a limit on the number of iterations. Regularization parameter $\alpha_k > 0$ is estimated at each iteration. Notice we now impose the fit to data term $\|\mathbf{Gm} - \mathbf{d}\|_2^2$, in a weighted norm, with diagonal weight matrix $(W_{\text{d}})_{ii} = 1/\sigma_i$ which has entries determined by an estimate of the variance of the noise in the $i^{\text{th}}$ data measurement, $\sigma_i^2$. The diagonal depth weighting $W_{\text{depth}}$ is also introduced. This matrix has entries determined by the depth coordinate $z_i$ for entry $i$ in $\mathbf{m}$, given by $(W_{\text{depth}})_{ii} = 1/z_i^\beta$, assuming that the surface is at depth 0 and depth values are calculated with the $z$ axis pointing down for positive values. Here $\beta = 0.8$ is chosen based on the model, as described in Li and Oldenburg (1998), Boulanger and Chouteau (2001) to be in the range [0.5, 1] for inversion of gravity data.[1] Weighting matrix $W^{(0)} = I$ is the identity matrix but is updated for $k > 0$ using a weighting determined by $r = 1$, specifically $W_{ii}^{(k)} = ((\mathbf{m}_i^{(k)} - \mathbf{m}_i^{(k-1)})^2 + \epsilon^2)^{1/4}$ when $r = 1$. Here $\epsilon^2$ is a small value taken to assure that no entry in $W^{(k)}$ is zero, and hence $W^{(k)}$ is invertible. Combining all terms and after some algebra we obtain $\mathbf{m}^{(k)}$ as $\mathbf{m}^{(k)} = (W^{(k)})^{-1}\mathbf{y}^{(k)} + \mathbf{m}^{(k-1)}$, where $\mathbf{y}^{(k)}$ solves the normal equations for the standard Tikhonov problem

$$\mathbf{y}^{(k)} = \underset{\mathbf{y}}{\operatorname{argmin}} \left\{ \left\|\mathbf{G}^{(k-1)}\mathbf{y} - \mathbf{r}^{(k-1)}\right\|^2 + \alpha_k^2 \|\mathbf{y}\|_2^2 \right\}. \tag{6}$$

Here system matrix $\mathbf{G}^{(k-1)} = W_{\text{d}}\mathbf{G}W_{\text{depth}}(\mathbf{W}^{(k-1)})^{-1}$ and residual $\mathbf{r}^{(k-1)} = W_{\text{d}}(\mathbf{d} - \mathbf{G}W_{\text{depth}}\mathbf{m}^{(k-1)})$ are updated at each step. In the experiments, we

---

[1] We note $\beta$ is replaced by $\beta/2$ and correspondingly approximately double values are suggested (Li and Oldenburg 1998).
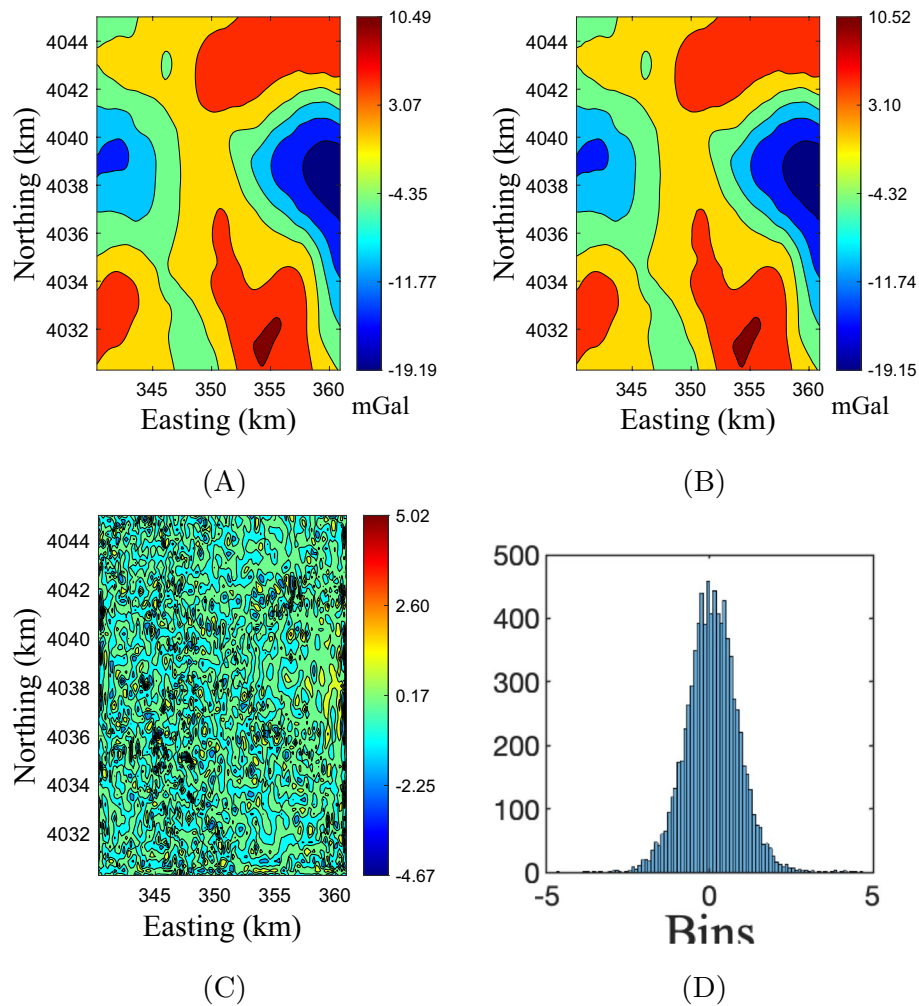
**Fig. 8 A** The residual anomaly for the data indicated as (a) in Fig. 3. **B** The residual anomaly predicted by the reconstructed model for region (a). **C** The weighted error of the map calculated from the subtraction of the predicted anomaly and the observed anomaly, weighted by the inverse covariance square root ($W_d$). **D** The graph shows the Gaussian histogram for the same weighted error

adjust the noise variance for the data so that the weighted residual for the prediction of the anomaly $W_d(\mathbf{d} - \mathbf{Gm}^{(K)})$ at final iteration $K$ is approximately normal with mean 0, as shown in the histograms (Figs. 8D and 9D) for the residuals. To find a suitable estimate we set $\sigma_i = \tau_1|\mathbf{d}_i| + \tau_2\|\mathbf{d}\|_1$, where $\tau_1$ and $\tau_2$ are adjusted (Renaut et al. 2020). The iteration is terminated either when $k = K_{\max}$, or when the $\chi^2$ estimate for the weighted residual $\|W_d(\mathbf{d} - \mathbf{Gm}^{(k-1)})\|_2^2 < m + \sqrt{2\,m}$ is achieved. Termination at $k = K_{\max}$ without satisfying the $\chi^2$ estimate is regarded as unsatisfactory. For real data it is standard to adjust the parameters $\tau_1$ and $\tau_2$ to obtain a good estimate of the noise distribution as performed here (Vatankhah et al. 2022. It can be seen in Table 1 that the variance in the data for region (a) is larger than for region (b), $\tau_1$ and $\tau_2$ are larger. This is keeping with the observed anomalies; the data for region (b) are much smoother than for region (a), and so the variance in the data is lower.
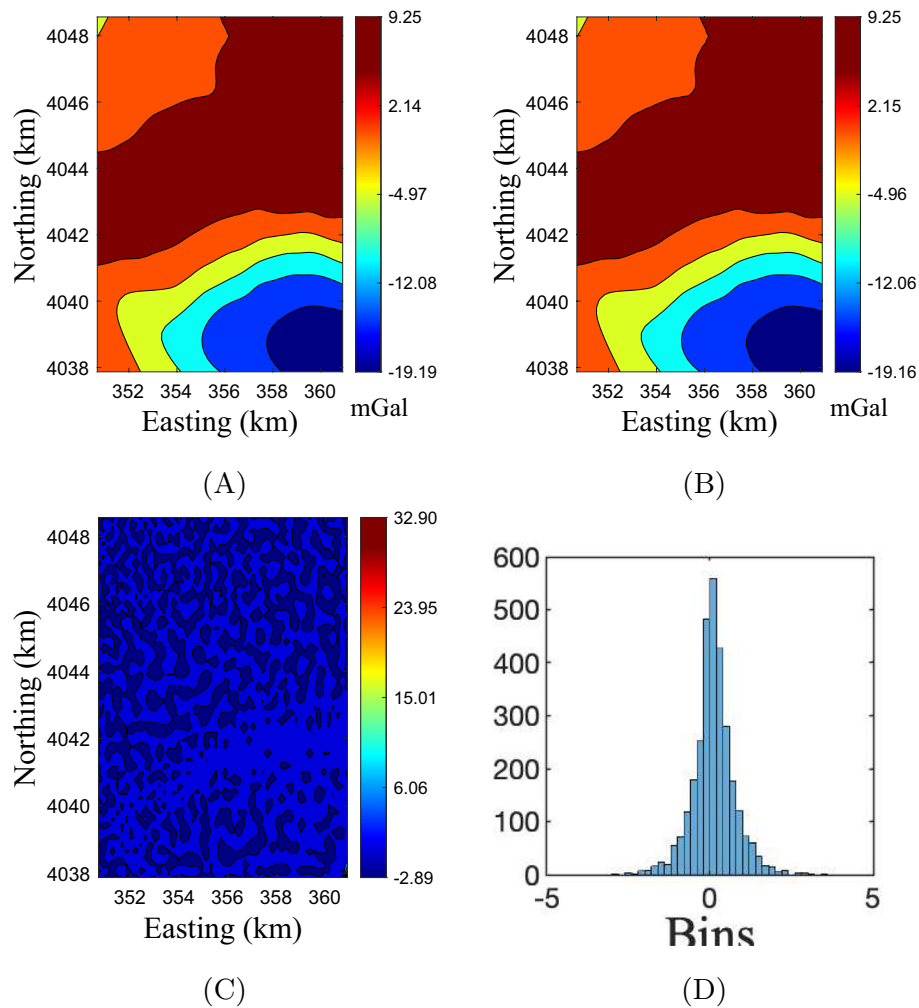
**Fig. 9 A** The residual anomaly for the data indicated as (b) in Fig. 3B. **B** The residual anomaly predicted by the reconstructed model for region (b). **C** The weighted error of the map calculated from the subtraction of the predicted anomaly and the observed anomaly, weighted by the inverse covariance square root ($W_d$). **D** The graph shows the Gaussian histogram for the same weighted error

The regularization parameter is obtained using the method of unbiased predictive risk estimation (UPRE) (Vatankhah et al. 2018; Vogel 2002) for $k > 0$ but is initialized as a large value at the first step $\alpha = (n/m)^{3.5}(s_1/\text{mean}(s(1:p)))$, where $s_i$ are the singular values for the dominant subspace for the matrix $\mathbf{G}^{(k-1)}$. Throughout we use the randomized singular value decomposition to obtain the solution of Eq. (6); this also provides the estimates for the singular values $s_i$ and the other components that are required for the UPRE method. Bound constraints on the density contrast are $-.35$ and $.3$ so that the calculated density contrast in the domain satisfies $-.35 \leq \Delta\rho \leq .30$, corresponding to the density for the structure imposed as $2.15 \leq \rho \leq 2.8$, assuming the background density is 2.5. These constraints are imposed at each iteration $k$ on $\mathbf{m}^{(k)}$ by projecting the data outside the range to the closest bound.

In our use of the randomized singular value decomposition, we use an oversampling percentage of 1% for the size of the projected domain, of size 1800 for region (a) and

1000 for region (b), corresponding to the over sampled spaces of sizes 1818 and 1010, respectively. The sizes of the projected spaces used in each case are chosen to provide efficiency in calculation by working with a projected size of the problem, while also capturing the dominant spectrum for the operator. Generally, a projected size near to $m/4$ is a compromise between cost and maintaining the dominant subspace. For these two regions we have a projected space of size $m/\ell$ where $\ell \approx 4.57$ and 2.99, respectively. Two power iterations are applied to obtain the projected space that provides the singular values, $s_1 \geq \ldots s_p > 0$ for the projected space of size $p$. For the $\chi^2$ estimate for the two regions we have $m + \sqrt{2m} = 8263.6$. and 3101.8, for $m = 8136$ and 3024, for regions (a) and (b) (delineated in Fig. 3B), respectively. The iteration proceeds so long as the estimate of the $\chi^2$ value is larger than the given bound for given $m$ and $k < K_{\max}$. Note $n = 272160$ and 104400 for these regions, larger than $mn_z$ because of the padding for the domain in East and North directions. Furthermore, the number of measurement stations for each domain, on the non-uniform grid, was 415 and 162, respectively. The data were interpolated to a regular grid for the BA and then further interpolated to provide a roughly uniform spacing for the inversion using the Matlab `scatteredInterpolant` function using the options for the natural cubic spline and a nearest neighbor interpolant for values falling just outside the grid.

In Table 2, we report the parameters describing the orientations of the cross sections and the depth slices. These are illustrated in Figs. 10 and 11, for the same total depth, but the extents of the regions in the East and North directions is determined by the sizes of regions (a) and (b) (delineated in Fig. 3B).

In the results (Figs. 8 and 9 for the anomalies, Fig. 12 for the volume structures), we see that the in their overlapping portion both inversions show a structural high (associated with a high density volume) with somewhat different details (Fig. 3B). This can be expected because the obtained structures are also impacted by the reconstruction of the volume for each complete region. The inversions show the existence of this structural high separating at depth the basin of Guelma from another basin to the northwest of Hammam Debagh. This second basin deepens to the southeast. Further, the inversions were repeated using depths of 12 km and 20 km. These results substantiate the major components of the subsurface structures illustrated in Fig. 12.

### The shallow subsurface structure

The energy spectrum obtained from the gravity field is illustrated in Fig. 6. Three main solutions are evident, corresponding to the different wavelengths (Fig. 6). A first packet represents the deepest generating sources that are located at more than 2.5 km. A second energy packet characterizes the superficial structures, with depths on the order of 0.2 km. These short wavelengths are associated with Neogene series, consisting of sandstone, limestone, marl and clay. A third energy packet shows intermediate depths (0.8 km) associated with the Cretaceous and Jurassic series comprising limestone, sandstone, clays, marls and quartzite associated with mineralization.

Figure 7 shows NE–SW clusters of Euler deconvolution solutions on the northern edge of the Guelma basin, with depths ranging between 1.5 and 2.2 km. The structure appears to juxtapose the E–W important strike-slip fault zone known as the northern limit of the basin. This E–W cluster is intersected by a NW–SE grouping which extends from
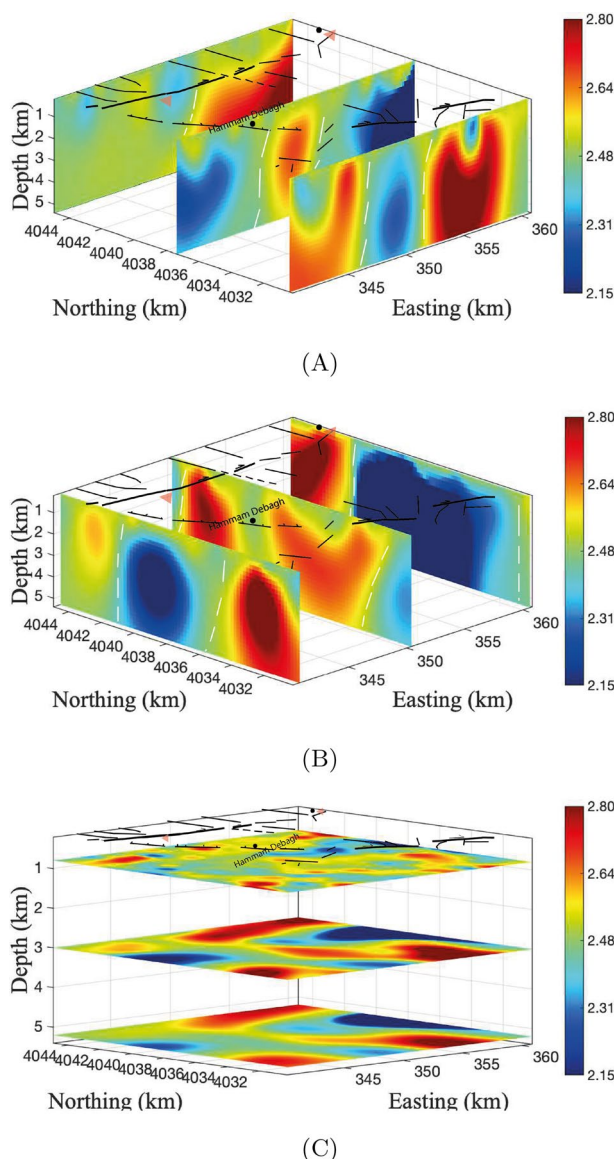
(A)



(B)



(C)

**Fig. 10** Cross sections and depth slices for the reconstructed model of region (a) in Fig. 3B. The levels are indicated in Fig. 2. East–West cross sections are shown in **A**. North–South sections are shown in **B**. Depth slices are shown in **C**. The black lines represent the geological faults in the area, the white lines infer faults that constitute high-permeability zones, the black points represent the hot spring locations, and the red triangles represent locations of significant mineralization

south of Guelma to Djebel Debagh (Debagh Mountain). This second cluster forms the western limit of the Guelma basin, with depth ranging from 0.8 to 1.5 km. This western edge of the Guelma basin is characterized by permanent superficial seismic activity. The Hammam Debagh area is characterized by a NW–SE cluster series with depth ranging from 0.3 km to 0.8 km. Frequently, seismicity can be considered as an indicator of geological faults that assist in identifying the hydrothermal systems and their associated pathways (Chacón-Hernández et al. 2021).

Several moderate earthquakes have struck the Guelma region and surroundings over many years, including for example Héliopolis on December 17, 1850 ($i_0$= VI EMS);
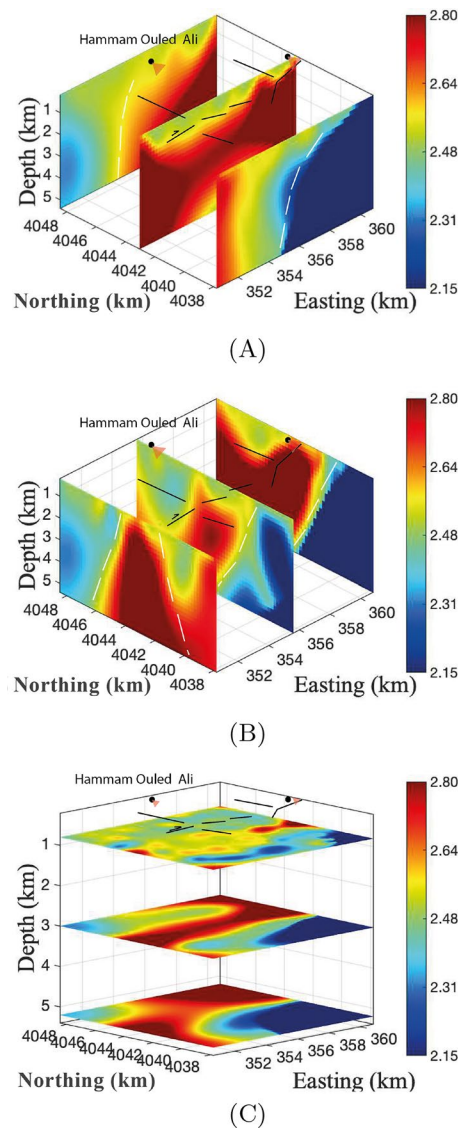
**Fig. 11** Cross sections and depth slices for the reconstructed model of region (b) in Fig. 3B. The levels are indicated in Fig. 2. East–West cross sections are shown in (**A**). North–South sections are shown in (**B**). Depth slices are shown in (**C**). The black lines represent the geological faults, the white lines infer faults that constitute high permeability zones, the black points represent the hot spring locations, and the red triangles represent locations of significant mineralization

**Table 1** Parameters used in the inversions with a maximal depth of 6 km

| $(n_{s_e}, de)$ | $(n_{s_n}, dn)$ | Origin | East | North | $(\tau_1, \tau_2)$ | $K$ | $\chi^2$ | mean |
|---|---|---|---|---|---|---|---|---|
| (108, 193) | (77, 194) | (340.2, 4030.2) | 20.8 | 14.9 | (0.001, 0.001) | 8 | 0.647 | 0.079 |
| (54, 193) | (56, 194) | (350.6, 4037.8) | 10.4 | 10.9 | (0.001, 0.0004) | 15 | 0.868 | 0.129 |

Data used in generating the solutions for each region are indicated in Table 1. The parameters of the first row correspond to region (a) of (Fig. 3), the second row gives the parameters used in the inversion of gravity data of region (b). Convergence was attained at $K$ iterations with the given $\chi^2$ values, for $n_{s_e}$ and $n_{s_n}$ stations in East and North directions. In both inversions we used 30 layers each 200 m thick, corresponding to a total depth of 6 km. Cells sizes in East and North directions are $de$ and $dn$. The choices for $n_{s_e}$ and $n_{s_n}$, and hence $de$ and $dn$ were made to obtain a grid that is close to 200m in each direction, for each region. The origin measured in the East-North coordinates for the region covered by the stations is given as Origin measured in km. The total dimensions of the domain measured in km, for the region covered by the stations, is given as East and North. The observed data are weighted with the given $\tau_1$ and $\tau_2$. Padding of 2 cells is applied in East and North directions. The mean value for the entries of the weighted residual for the prediction of the observed data is given as mean

**Table 2** Coordinates for the slices using a model extending to 6 km in depth

| Region | East | North | Depth |
|---|---|---|---|
| (a) | (340.75, 350.39, 360.62) | (4030.39, 4037.36, 4044.92) | (0.80, 3.00, 5.20) |
| (b) | (350.59, 355.60, 360.81) | (4037.77, 4043.02, 4048.47) | (0.80, 3.00, 5.20) |

The coordinates of the N–S and E–W cross sections, and the depths of the slices are summarized in Table 2 for regions (a) and (b) (delineated in Fig. 3B) given in km. The slices are chosen to the closest measurement on the specific grid, which depends on the East and North directions, as indicated in Table 1



(A)



(B)
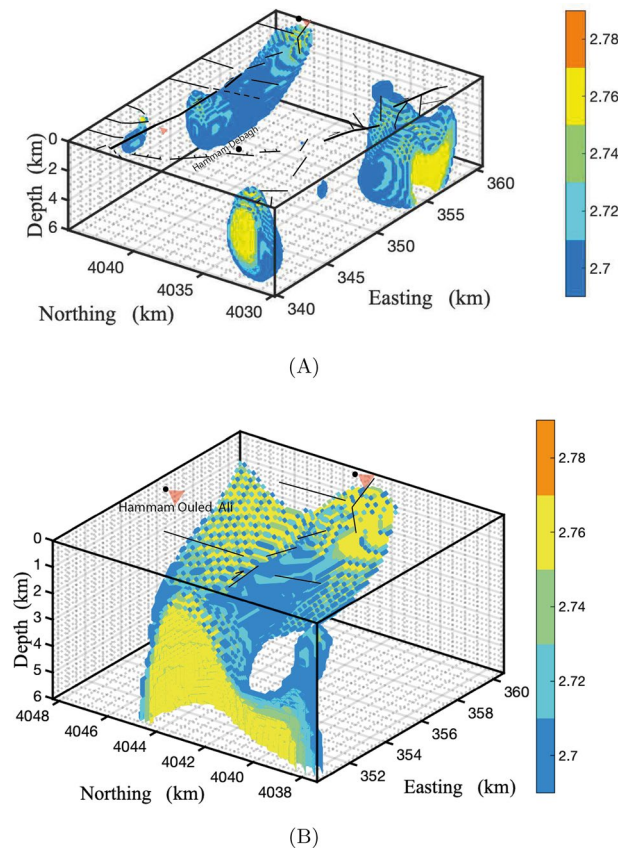
**Fig. 12** 3D volume of the anomalies with high density. **A** represents the shape of anomalies with high density in the first area (a) (Fig. 3). **B** highlights the shape of anomalies with high density in the second area (b) (Fig. 3). The black lines represent the possible geological faults into the area, the black points represent the hot spring locations, and the red triangles represent locations of significant mineralization

Guelma on February 10, 1937 ($i_0$= VIII EMS, mb = 5.4); and recently Hammam Debagh on September 20, 2003 (Mw = 5.2) with a normal fault mechanism. According to several authors (Meghraoui and Pondrelli 2012; Abbassene et al. 2016; Saibi 2009) the NNW–SSE Roknia–Hammam Debagh hydrothermal sources alignment has neotectonic significance and seems to be related to an NW–SE active fault. This can be confirmed by the good correlation between the gravimetric data and the fault orientation observed in the field (Maouche et al. 2013). The 2003 focal mechanism solution and the trends of the geomorphic structures correlate with the hydrothermal sites.

The 3D density models obtained from the independent inversions of the residual anomalies for regions (a) and (b) clearly demonstrate that there are three main

high-density rock zones. Region (a) (Fig. 10) indicates the presence of a significant high-density zone located in the southwestern part of the map (close to Hammam Debagh). It has an average density of about 2780 kg/cm$^3$ (Fig. 10), originates at a depth ranging from about 500 m to an average depth of about 4000 m, and extends in depth to about 5400 m where the density is about 2740 kg/cm$^3$. The second anomaly in region (a) is located in the south central part of the inversion area. It is considered more significant due to its vast size. The average density for this zone is around 2780 kg/cm$^3$ focused in the middle of the anomaly. This high-density zone is estimated to originate at about 3600 m and extends to more than 6000 m with an average density of about 2760 kg/cm$^3$, starting from about 500 m in depth. It is located south of the Debagh mountain. The third anomaly observed is located along the northern part of region (a). It has an important E–W elongated shape and has a density that ranges between 2700 and 2780 kg/cm$^3$. The depth is considered more significant. It ranges between 6000 m and 3000 m from East to West. The maximum depth for these zones is in the north west of the region (b), which is close to both geothermal systems (Hammam Debagh and Ouled Ali). This density change shown in the models is a significant contribution; it highlights the availability of a pathway for water upflow.

Region (b) (Fig. 11) indicates a primary anomaly that occupies the northern and western portion of zone (b) and is elongated E–W. This anomaly has been shown before, but further details are highlighted for this smaller region. It was selected to also enclose the northern part of the study area, where Hammam Ouled Ali is located. The inversion indicates that the density ranges between 2700 and 2780 kg/cm$^3$ (Fig. 11) and that the depth of this high-density zone extends to more than 6000 m in the western and eastern portions of this area. The depth is estimated to be about 3000 m in the central part of the map. In the southern E–W density section, we notice the low-density rock associated with the Guelma basin. Going through to the west, the central anomaly delimits the basin to the north. This high-density zone is associated with the Bousbaa Mountain. The fault limiting the high and low-density zone has a high-permeability zone through which the geothermal brines can ascend to the surface.

Overall, the 3D models for the two regions (a) and (b) (delineated in Fig. 3B), as shown by cross section and depth slices in Figs. 10 and 11, are highlighted by the volume representation shown in Fig. 12 for the high-density zones. Primarily, the southern limit of the northern high-density zone correlates with the hydrothermal systems in the area (Hammam Debagh, Hammam Ouled Ali). From the first map (Fig. 12A) we observe the presence of two zones in the eastern region with significant depths. The first, located in the northeastern portion of the region, exists in both figures (Fig. 12A and B). The average density of these zones is 2720 kg/cm$^3$. It is located predominantly under Hammam Ouled Ali and Djebel Bousbaa (Bousbaa Mountain), the shape of this high-density zone is illustrated in (Fig. 12B), where we can clearly see its depth extension. The southern limit of the northern high-density zone correlates with the hydrothermal systems in the area of Hammam Debagh and Hammam Ouled Ali. It also dominates the overlapping portion of region (b). The other zone in the southwestern part of the map (Fig. 12A) has an average density around 2740 kg/cm$^3$ and is situated chiefly under the Hammam Debagh hydrothermal systems.

## Hydrothermal systems controlled by faults

The information revealed from the gravity data along the surrounding area of the Guelma basin, particularly, the Hammam Debagh and Hammam Ouled Ali area, helps to understand the geothermal systems in the region (Figs. 2, Fig. 3A, Fig. 5A, B). Specifically, hot spring systems lie beneath the geophysically interpreted faults. According to our qualitative and quantitative analyses, the hot springs lie around the traces of faults that correlate with the limits of high and low-density zones.

The results obtained from the 3D-Euler deconvolution correlate reasonably well with the gravimetric lineaments obtained from the gradients maps and also with the physical faults mapped by geology. The hydrothermal system of Hammam Debagh and Hammam Ouled Ali is illustrated by springs located at fissures. Along these fractures and faults the flows of these hot springs (thermo-mineral) generate the travertine deposits that are charged with carbonates. The distribution of hydrothermal manifestations is strongly controlled by the well-developed structural tissue and the important temperature values at the emergence of thermal springs explained by a high geothermal gradient. The temperatures of the thermal waters of these systems range from 20 to 97 ℃. Considering the normal geothermal gradient of 1° C per 30 m in depth (Ouali et al. 2006), and deeming the energy dissipation related to the upwelling, the results suggest that this water comes from depths exceeding 2400 m. The geothermal systems in the area are divided by the Hammam Debagh fault. The local seismic activity is related to the presence of several faults that are considered significant for conveyance of, and control the cooling of, hot water.

The density model of both areas reveals the presence of high-density bodies, mostly located under the spring water. These high-density bodies are interspersed with low-density bodies. The limits between these high and lower density bodies constitute faults that are, the pathway that allows the upflow of heat buoyant geothermal fluids from the deeper zone of the crust. The gravimetric lineaments directions highlighted by the horizontal and vertical gradients are practically coherent with the fault orientation revealed from the region, the gravimetric lineament elongated E–W is slightly juxtaposed on the major fault of Hammam Debagh. The structural investigation has revealed minors fault structures in the NNW–SSE direction, with apparent normal movement outcropping in Miocene, Pliocene sandstones, and travertine (Maouche et al. 2013). The main mineral deposits in this region are located along the E–W and NE–SW faults, which play a major role in the emplacement of mineralization (Amara et al. 2019). The interpretation of the results strongly suggests that the hydrothermal systems (Hammam Debagh and Ouled Ali) are articulated around faults as zones of high permeability located in the same place as the travertine walls. The Hammam Debagh fault system responsible for this collapse has caused failures in the blocks which are delimited and connected to the Djebel Debagh dextral fault and southern Guelma Strike Slip fault (Bendjama et al. 2021). The recent activity of this fault is attested to by the moderate earthquakes that have occurred in this zone. The seismicity that has been observed in this study area could be related to the geothermal activity such as in the Tres Virgenes geothermal field in Mexico and elsewhere. This gravimetric study has established that the site basement is affected by faults and fractures that constitute flow paths

for thermal waters, allowing them to ascend to the surface. This can be explained by high temperatures of the thermal waters of these systems. A gravimetric study of this kind is a powerful tool that can contribute to defining the fracture pattern in the basement of the hydrothermal system area.

## Conclusion

The Guelma region is known for its different outcrops and complex geology. This latter is of significant relevance for improving our understanding of the geology and to better extract the shape of the related geothermal systems. The gravity survey carried out in this area provides information that contributes information (faults delimiting the basins, etc.) to our understanding of the hydrothermal features in the region. The application of the residual filter helps highlight the shallow anomalies in the area, and the use of the horizontal gradient showcases the gravimetric lineaments and the links created between them. The 3D-Euler deconvolution assists with quantifying the depth of several faults existing in the Hammam Debagh and Hammam Ouled Ali regions, and confirms the correlation between the gravimetric lineaments and the faults existing in the region. Finally, the energy spectrum provides information about the depths of the gravity anomalies, and the inversion of the gravity data yields the shapes of the high-density anomalies that are dispersed in the main area. The random location of the high-density bodies confirms that the region is geologically complex. The upflow of the geothermal waters through the high-permeability zones depicted in our 3D gravity model suggests a geothermal system originating at a heat source deep in the crust. The geological heterogeneity of this region revealed from the gravity inversion provides a better understanding of the permeability zones available between these high and low-density bodies, and the sedimentary and metamorphic rocks in the area play a significant role in providing the spaces between these bodies. The geothermal system in the study area illustrates a critical water temperature. This water derives its high-temperature from deep in the crust and interacts geochemically during this upflow with the rocks along the upflow pathway. These large high-density bodies are linked with each other due to active fault structures in the area. Furthermore, the gradient geothermic has a significant position in this hydrothermal system. The Hammam Debagh fault is considered the principal escape for the water flow. This fault is located in the middle of the study area and splits the area into two parts. The study revealed that the Hammam Debagh fault contains other linked minor faults that reach the surface. These links allow the water to reach the surface at a high temperature and the network allows the fast flow of hot water in several places in the study area.

## Declarations

**Competing interests**
The authors declare that they have no competing interests.

## References

Abbassene F, Chazot G, Bellon H, Bruguier O, Ouabadi A, Maury RC, Déverchére J, Bosch D, Monié P. A 17Ma onset for the post-collisional K-rich calc-alkaline magmatism in the Maghrebides: evidence from Bougaroun (northeastern Algeria) and geodynamic implications. Tectonophysics. 2016;674:114–34.
Alatorre-Zamora MA, Enriquez JOC, Fregoso E, Belmonte-Jiménez SI, Chávez-Segura R, Gaona-Mota M. Basement faults deduction at a dumpsite using advanced analysis of gravity and magnetic anomalies. Near Surface Geophys. 2020;18(3):307–31.
Amara BN, Aissa DE, Maouche S, Braham M, Machane D, Guessoum N. Hydrothermal alteration mapping and structural features in the Guelma Basin (Northeastern Algeria): contribution of Landsat-8 data. Arabian J Geosci. 2019;12(3):94.
Armadillo E, Rizzello D, Pasqua C, Pisani P, Ghirotto A, Kabaka K, Mnjokava T, Mwano J, Didas M, Tumbu L. Geophysical constraints on the Luhoi (Tanzania) geothermal conceptual model. Geothermics. 2020;87:101875.
Aydogan D. Extraction of lineaments from gravity anomaly maps using the gradient calculation: application to Central Anatolia. Earth Planet Space. 2011;63(8):903–13.
Baranov V. Calcul du gradient vertical du champ de gravité ou du champ magnétique mesuré à la surface du sol. Geophys Prospect. 1953;1(3):171–91.
Basantaray AK, Mandal A. Interpretation of gravity-magnetic anomalies to delineate subsurface configuration beneath east geothermal province along the Mahanadi rift basin: a case study of non-volcanic hot springs. Geotherm Energy. 2022;10(1):1–27.
Bayou Y, Bouyahiaoui B, Berguig MC, Abtout A. The new gravimetric network of the north-eastern part of Algeria. Heliyon. 2022. https://doi.org/10.1016/j.heliyon.2022.e10455.
Belhai M, Fujimitsu Y, Bouchareb-Haouchine FZ, Nishijima J. Geology, geothermometry, isotopes and gas chemistry of the Northern Algerian geothermal system. Geology. 2015;19:25.
Bendali M, Abtout A, Bouyahiaoui B, Boukerbout H, Marok A, Reolid M. Interpretation of new gravity survey in the seismogenic Upper Chelif Basin (North of Algeria): deep structure and modeling. J Iber Geol. 2022. https://doi.org/10.1007/s41513-022-00190-7.
Bendjama H, Yelles-Chaouche A, Boulahia O, Abacha I, Mohammedi Y, Beldjoudi H, Rahmani ST-E, Belheouane O. The March 2017 earthquake sequence along the EW-trending Mcid Aïcha-Debbagh Fault, northeast Algeria. Geosci J. 2021;25(5):697–713.
Bhattacharyya Bo Ko, Chan KC. Reduction of magnetic and gravity data on an arbitrary surface acquired in a region of high topographic relief. Geophysics. 1977;42(7):1411–30.
Blakely RJ. Potential theory in gravity and magnetic applications. Cambridge: Cambridge University Press; 1995.
Bouaicha F, Dib H, Bouteraa O, Manchar N, Boufaa K, Chabour N, Demdoum A. Geochemical assessment, mixing behavior and environmental impact of thermal waters in the Guelma geothermal system, Algeria. Acta Geochim. 2019;38(5):683–702.
Bouchareb-Haouchine FZ, Boudoukha A, Haouchine A. Hydrogéochimie et géothermométrie: apports à l'identification du réservoir thermal des sources de Hammam Righa, Algérie. Hydrol Sci J. 2012;57(6):1184–95.
Boulanger O, Chouteau M. Constraints in 3D gravity inversion. Geophys Prospect. 2001;49(2):265–80.
Bousquet B. Tectonique et quaternaire moyen en Méditerranée (tectonics and the middle Quaternary in the Mediterranean). Bulletin de l'Association de Géographes Français. 1986;63(1):31–45.

Bouyahiaoui B, Sage F, Abtout A, Klingelhoefer F, Yelles-Chaouche K, Schnürle P, Marok A, Déverchère J, Arab M, Galve A, et al. Crustal structure of the eastern Algerian continental margin and adjacent deep basin: implications for late Cenozoic geodynamic evolution of the western Mediterranean. Geophys J Int. 2015;201(3):1912–38.

Bouyahiaoui B, Abtout A, Hamai L, Boukerbout H, Djellit H, Bougchiche SS, Bendali M, Bouabdallah H. Structural architecture of the hydrothermal system from geophysical data in Hammam Bouhadjar area (northwest of Algeria). Pure Appl Geophys. 2017;174(3):1471–88.

Chacón-Hernández F, Zúñiga FR, Enriquez JOC, Lermo-Samaniego J, Jiménez-Méndez N. Analysis of shear wave splitting anisotropy in the Tres Virgenes Volcanic Complex, Baja California Sur. Mexico Geothermics. 2021;94:102–15.

Dickson MH, Fanelli M. Geothermal energy: utilization and technology. New York: Routledge, Earthscan; 2013.

Elbarbary S, Zaher MA, Saibi H, Fowler A-R, Saibi K. Geothermal renewable energy prospects of the African continent using GIS. Geotherm Energy. 2022;10(1):1–19.

Enriquez JOC, Thomann J, Goupillot M. Applications of bidimensional spline functions to geophysics. Geophysics. 1983;48(9):1269–73.

Florio G, Fedi M. Multiridge Euler deconvolution. Geophys Prospect. 2014;62(2):333–51.

Francis O. Réseau de gravimétrie absolue Algérien. Bulletin des Sciences Géographiques. 2003;9(Avril):3–9.

Gibert D, Galdeano A. A computer program to perform transformations of gravimetric and aeromagnetic surveys. Comput Geosci. 1985;11(5):553–88.

Hogue JD, Renaut RA, Saeed Vatankhah S. A tutorial and open source software for the efficient evaluation of gravity and magnetic kernels. Comput Geosci. 2020;14:104575.

Jean-Claude L. Les séries ultratelliennes d'Algérie nord-orientale et les formations environnantes dans leur cadre structural. PhD thesis, Toulouse; 1987.

Johnson A, Macleod I. Using power spectra for potential field data interpretation: challenges and cautions. J Geophys. 2016;37:187–90.

Kearey P, Brooks M, Hill I. An introduction to geophysical exploration, vol. 4. Singapore: John Wiley & Sons; 2002.

Lebbihiat N, Atia A, Arıcı M, Meneceur N. Geothermal energy use in Algeria: a review on the current status compared to the worldwide, utilization opportunities and countermeasures. J Clean Prod. 2021;302:126950.

Leseane K, Atekwana EA, Mickus KL, Abdelsalam MG, Shemang EM, Atekwana EA. Thermal perturbations beneath the incipient Okavango Rift Zone, northwest Botswana. J Geophys Res Solid Earth. 2015;120(2):1210–28.

Li Y, Oldenburg DW. 3-D inversion of gravity data. Geophysics. 1998;63(1):109–19.

Maouche S, Meghraoui M, Morhange C, Belabbes S, Bouhadad Y, Haddoum H. Active coastal thrusting and folding, and uplift rate of the Sahel Anticline and Zemmouri earthquake area (Tell Atlas, Algeria). Tectonophysics. 2011;509(1–2):69–80.

Maouche S, Abtout A, Merabet N-E, Aïfa T, Lamali A, Bouyahiaoui B, Bougchiche S, Ayache M. Tectonic and hydrothermal activities in Debagh, Guelma Basin (Algeria). J Geol Res. 2013. https://doi.org/10.1155/2013/409475.

Meghraoui M, Pondrelli S. Active faulting and transpression tectonics along the plate boundary in North Africa. Annal Geophys. 2012;55(5):955.

Meghraoui M. Géologie des zones sismiques du Nord de l'Algérie: Paléosismologie, tectonique active et synthèse sismotectonique. PhD thesis, Paris 11; 1988.

Melo F, Barbosa V. Base-level estimates to define the correct structural index in Euler deconvolution. In: 2017 SEG International Exposition and Annual Meeting, OnePetro; 2017. pp. 1770–5.

Mickus KL, Aiken CLV, Kennedy WD. Regional-residual gravity anomaly separation using the minimum-curvature technique. Geophysics. 1991;56(2):279–83.

Mikhailov V, Galdeano A, Diament M, Gvishiani A, Agayan S, Bogoutdinov S, Graeva E, Sailhac P. Application of artificial intelligence for Euler solutions clustering. Geophysics. 2003;68(1):168–80.

Oldham CHG, Sutherland DB. Orthogonal polynomials: their use in estimating the regional effect. Geophysics. 1955;20(2):295–306.

Ouali S, Khellaf A, Baddari K. Etude géothermique du Sud de l'Algérie. Revue des Énergies Renouvelables. 2006;9(4):297–306.

Ouali S, Hadjiat MM, Ait-Ouali A, Salhi K, Malek A. Cartographie et caractérisation des resources géothermiques de l'Algérie. J Renew Energ. 2018;21(1):54–61.

Peacock JR, Earney TE, Mangan MT, Schermerhorn WD, Glen JM, Walters M, Hartline C. Geophysical characterization of the Northwest Geysers geothermal field, California. J Volcanol Geotherm Res. 2020;399:106882.

Raoult J-F. Geologie du center de la Chaine Numidique (nord du Constantinois), Algerie. Société géologique de France Language; 1974.

Reid AB, Thurston JB. The structural index in gravity and magnetic interpretation: Errors, uses, and abuses. Geophysics. 2014;79(4):J61–6.

Reid AB, Allsop JM, Granser H, Millett AJ, Somerton IW. Magnetic interpretation in three dimensions using Euler deconvolution. Geophysics. 1990;55(1):80–91.

Renaut RA, Hogue JD, Vatankhah S, Liu S. A fast methodology for large-scale focusing inversion of gravity and magnetic data using the structured model matrix and the 2D fast Fourier transform. Geophys J Int. 2020;223(2):1378–97.

Risacher F, Fritz B, Hauser A. Origin of components in Chilean thermal waters. J South Am Earth Sci. 2011;31(1):153–70.

Saibi H. Geothermal resources in Algeria. Renew Sustain Energy Rev. 2009;13(9):2544–52.

Said M, Youcef B, Assia H, Yasmina R, Farida O, Abdelhakim A. Active tectonics and seismic hazard in the Tell Atlas (Northern Algeria): a review. In: Bendaoud A, Hamimi Z, Hamoudi M, Djemai S, Zoheir B, editors. The geology of the Arab world–an overview. Cham: Springer; 2019. p. 381–400.

Salem A, Ravat D. A combined analytic signal and Euler method (AN-EUL) for automatic interpretation of magnetic data. Geophysics. 2003;68(6):1952–61.

Spector A, Grant FS. Statistical models for interpreting aeromagnetic data. Geophysics. 1970;35(2):293–302.

Thompson DT. EULDPH: a new technique for making computer-assisted depth estimates from magnetic data. Geophysics. 1982;47(1):31–7.

Vatankhah S, Renaut RA, Ardestani VE. A fast algorithm for regularized focused 3-D inversion of gravity data using the randomized SVD. Geophysics. 2018;83:G25–34.

Vatankhah S, Renaut RA, Huang X, Mickus K, Gharloghi M. Large-scale focusing joint inversion of gravity and magnetic data with Gramian constraint. Geophys J Int. 2022;230(3):1585–611.

Vila J-M. La chaîne alpine de l'Algérie orientale et des confins Algéro-Tunisiens. These de Doctorat-es-sciences, Universite Pierre et Marie curie; 1980.

Vogel C. Computational methods for inverse problems. Society for Industrial and Applied Mathematics, Philadelphia; 2002.

Yelles-Chaouche AK, Boudiaf A, Djellit H, Bracene R. La tectonique active de la région nord-Algérienne. Comptes Rendus Geosci. 2006;338(1–2):126–39.

Zhao X, Zeng Z, Yangang W, He R, Qiong W, Zhang S. Interpretation of gravity and magnetic data on the hot dry rocks (HDR) delineation for the enhanced geothermal system (EGS) in Gonghe town, China. Environ Earth Sci. 2020;79(16):1–13.

**Publisher's Note**

Springer Nature remains neutral with regard to jurisdictional claims in published maps and institutional affiliations.